A Multi-Scale Hybrid Model of CSC Emergence Through IL-6 Signaling: Integrating GRNs into Agent-Based Tumor Simulations

Mahule Roy[1,2,3,*], Subhas Roy[4]

[1]University of Oxford

[2]Harvard Medical School

[3]Brigham and Women's Hospital, Boston

[4]TATA Consumer Products Limited

*Corresponding author: mroy25@bwh.harvard.edu

Abstract

Cancer stem cells (CSCs) represent a critical subpopulation within tumors that drive metastasis, therapeutic resistance, and post-treatment recurrence. While interleukin-6 (IL-6) signaling has been established as a key mediator in the conversion of non-stem cancer cells (NSCCs) to CSCs, existing computational models predominantly focus on sustained cytokine expression patterns. Emerging experimental evidence suggests that IL-6 secretion often occurs in transient, pulsatile bursts under stress conditions such as hypoxia, chemotherapy, or chronic inflammation. This study develops a multi-scale hybrid computational model to investigate how temporal dynamics of IL-6 signaling—specifically pulsed versus sustained patterns—influence CSC emergence through the LIN28–let-7 regulatory axis. We constructed a gene regulatory network (GRN) incorporating IL-6, NF-ϰB, LIN28, let-7, c-Myc, and OCT4, modeled via ordinary differential equations (ODEs) with shifted Hill functions to capture nonlinear regulatory interactions. This intracellular GRN was integrated into a multicellular agent-based framework using CompuCell3D, enabling simulation of tumor population dynamics under spatially heterogeneous cytokine fields. We systematically compared four signaling regimes: (1) pulsed IL-6 with sustained NF-ϰB, (2) sustained IL-6 with sustained NF-ϰB, (3) stochastic IL-6 with sustained NF-ϰB, and (4) pulsed IL-6 with pulsed NF-ϰB. Our simulations reveal that transient IL-6 pulses, particularly when synchronized with NF-ϰB activation, promote more robust and dynamic CSC emergence compared to sustained or stochastic signaling patterns. The coordinated pulsing enhanced bistable switch activation frequency, pushing more NSCCs across the stemness threshold defined by OCT4 expression. These findings suggest that cytokine temporal dynamics represent a critical determinant of tumor plasticity and propose pulsed microenvironments as potential accelerators of stem-like transitions. This work provides a novel computational framework for studying cytokine dynamics in tumor evolution and offers insights for therapeutic strategies targeting CSC emergence.

1 Introduction

Cancer stem cells (CSCs) constitute a functionally distinct subpopulation within tumors characterized by self-renewal capacity, multilineage differentiation potential, and enhanced resistance to conventional therapies. These cells are primarily responsible for long-term tumor propagation, metastasis, and post-treatment relapse, making them a critical focus in oncology research [1]. While CSCs were initially considered a static population, accumulating evidence demonstrates that non-stem cancer cells (NSCCs) can spontaneously convert to CSCs under specific microenvironmental conditions, particularly those involving inflammatory or stress signals [2, 3]. This phenotypic plasticity represents a dynamic, regulated process governed by molecular networks that modulate cellular stemness.

Interleukin-6 (IL-6) is a pleiotropic cytokine with established roles in immune regulation, inflammation, and cancer progression. Within tumor microenvironments, IL-6 is secreted by both malignant and stromal cells in response to various stressors, including hypoxia, chemotherapy, and mechanical stress. IL-6 signaling activates the NF-$\varkappa$B/STAT3 axis, which subsequently upregulates key stemness factors such as OCT4 and LIN28 [10, 11]. This molecular cascade positions IL-6 as a critical mediator of CSC induction. However, current computational models predominantly simulate IL-6 as a sustained, constant signal, overlooking emerging biological evidence that IL-6 secretion often occurs in transient, pulsatile bursts during stress conditions [12,13]. The role of such temporal dynamics in CSC emergence, particularly through the LIN28–let-7 regulatory axis, remains inadequately characterized.

This study addresses this knowledge gap by developing a multi-scale hybrid computational model that integrates gene regulatory network (GRN) dynamics with agent-based tumor simulations. We focus on the LIN28–let-7 mutual inhibition toggle switch, which functions as a bistable circuit regulating stemness transitions. OCT4, a transcription factor crucial for maintaining pluripotency, serves as a quantitative marker defining a "stemness window"—a specific range of OCT4 expression that facilitates phenotypic switching from NSCC to CSC states [4]. Our model investigates how different temporal patterns of IL-6 signaling (pulsed, sustained, and stochastic) influence the activation of this stemness window and subsequent CSC emergence.

2 Materials and Methods

2.1 Gene Regulatory Network Design and Justification

The core gene regulatory network (GRN) governing stemness transitions was constructed based on extensive literature review of established biological mechanisms (Figure 6). The network integrates IL-6, NF-$\varkappa$B, LIN28, let-7 microRNA, c-Myc, and OCT4, forming a tightly interconnected regulatory circuit. This design draws from multiple foundational studies: the stemness window model proposed by Jolly et al. (2015) provides the OCT4-

centric framework for phenotypic switching; the IL-6–NF-ϰB–LIN28–let-7 circuit identified by Iliopoulos et al. (2009) establishes the inflammation-stemness connection; the inflammation-induced bistability model from Gerard et al. (2014) informs the nonlinear dynamics; and insights from Girel et al. (2021) on cell division stochasticity contribute to population-level heterogeneity.

In this GRN, stress signals within the tumor microenvironment trigger IL-6 secretion, which subsequently activates NF-ϰB. Activated NF-ϰB upregulates LIN28 expression while simultaneously suppressing let-7 microRNA. LIN28 and let-7 form a mutual inhibitory feedback loop that functions as a bistable toggle switch, dictating cellular fate decisions. Let-7 inhibits stemness by repressing both c-Myc and LIN28, while LIN28 promotes stemness by inhibiting let-7 and activating OCT4. OCT4 expression, which depends solely on LIN28 levels in our simplified model, determines entry into the stemness window (0.2–0.6 normalized units), triggering transition from NSCC to CSC phenotypes.

2.2 Ordinary Differential Equation Modeling

The GRN was translated into a system of ordinary differential equations (ODEs) to simulate continuous, time-dependent molecular dynamics. Hill functions were employed to capture the sigmoidal activation and inhibition characteristics typical of biological regulatory interactions. The general form of shifted Hill functions used in our model is:

$$H^s(X) = H^-(X) + \lambda H^+(X) \tag{1}$$

where λ represents a fold change in gene expression. A special property of these functions, derived from Jolly et al. (2014), simplifies computational implementation:

$$H^s(X,3) = H^-(X) + 3H^+(X) = 1 + 2H^+(X), \text{ since } H^-(X) + H^+(X) = 1 \tag{2}$$

The specific ODEs governing key molecular species include:

$$\frac{d[\text{IL-6}]}{dt} = S(t) - \delta_{IL6}[\text{IL-6}] \tag{3}$$

$$\frac{d[\text{NF-}\varkappa\text{B}]}{dt} = \alpha_{NF} H^+([\text{IL-6}]) - \delta_{NF}[\text{NF-}\varkappa\text{B}] \tag{4}$$

$$\frac{d[\text{LIN28}]}{dt} = \alpha_L H^+([\text{NF-}\varkappa\text{B}]) \cdot H^-([\text{let-7}]) - \delta_L[\text{LIN28}] \tag{5}$$

$$\frac{d[\text{let-7}]}{dt} = \alpha_l H^-([\text{LIN28}]) - \delta_l[\text{let-7}] - \beta_l H^+([\text{NF-}\varkappa\text{B}])[\text{let-7}] \tag{6}$$

$$[\text{OCT4}] = H^+([\text{LIN28}], n_{OCT4}, K_{OCT4}) \tag{7}$$

Parameter values were extracted from experimental literature where available, including half-lives of IL-6 and let-7 from Marotta et al. (2011). Remaining parameters were estimated from prior computational models (Jolly et al., 2014; Gerard et al., 2014) or through logical reasoning and fitting, particularly for pulse amplitude and duration specifications.

2.3 Integration with Agent-Based Modeling Framework

To simulate emergent multicellular behavior, the GRN was integrated into an agent-based modeling framework using CompuCell3D version 4.2.0. Each cell was treated as an autonomous agent containing an identical internal GRN structure but exposed to spatially and temporally variable IL-6 levels within the simulated microenvironment. The integration pipeline utilized Tellurium to convert ODEs written in Antimony format into SBML files, which were then imported into CompuCell3D using the SBMLSolver module. This approach enabled each cell to solve its GRN locally while participating in population-level dynamics.

Two distinct cell types were defined within the simulation: (1) Non-Stem Cancer Cells (NSCCs), representing the default proliferative state capable of fate transition; and (2) Stem Cancer Cells (SCCs), exhibiting stem-like phenotypes with increased plasticity and growth potential. Custom steppables implemented in C++ were developed to control specific aspects of the simulation:

- **IL6PulseSteppable**: Simulated transient, pulse-like IL-6 secretion localized to NSCCs during an early time window (typically the first 200 Monte Carlo Steps), emulating acute inflammatory bursts.

- **IL6SustainedSteppable**: Implemented continuous IL-6 secretion across all NSCCs, leading to progressive cytokine accumulation and spatial saturation.

- **IL6StochasticSteppable**: Introduced probabilistic IL-6 release with tunable secretion probability ($\rho = 0.3$), resulting in spatiotemporal heterogeneity mimicking noisy or microenvironmentally modulated cytokine fields.

- **NFkBPulseSteppable**: Provided temporally limited NF-ϰB activation synchronized with IL-6 pulses, enabling investigation of signaling coincidence and transient synergy.

- **NFkBSustainedSteppable**: Applied constant NF-ϰB activation (35,000 arbitrary units) across all NSCCs throughout the simulation, mimicking chronic inflammation or constitutive pathway activation.

Cell behaviors were regulated through additional steppables: `GrowthSteppable` adjusted cell growth rates based on type, `MitosisSteppable` triggered division once cell volume exceeded a predefined threshold, and `GRNExecutionSteppable` executed the GRN for each NSCC, computed OCT4 levels, and triggered stochastic fate switching to SCCs when OCT4 values fell within the stemness window ($0.2 \leq \text{OCT4} \leq 0.6$).

2.4 Parameter Estimation and Model Calibration

2.4.1 Parameter Estimation Methodology

Unknown parameters were estimated using a multi-objective optimization framework. The objective function minimized the sum of squared errors between model predictions and three experimental datasets: (1) IL-6-induced OCT4 dynamics from Jolly et al. (2015), (2) LIN28-let-7 mutual inhibition kinetics from Iliopoulos et al. (2009), and (3) NF-ϰB activation profiles from Gerard et al. (2014). Optimization employed the Nelder-Mead simplex algorithm with bound constraints (Supplementary Table S2). Each parameter was initialized within physiologically plausible ranges derived from literature surveys.

2.4.2 Goodness-of-Fit Assessment

Model fit was quantified using multiple metrics:

- **R**^{2}: 0.87 for OCT4 dynamics, 0.79 for LIN28-let-7 oscillations
- **Akaike Information Criterion (AIC)**: -142.3 (compared to alternative models)
- **Bayesian Information Criterion (BIC)**: -128.7
- **Root Mean Square Error (RMSE)**: 0.034 normalized units

The AIC weights indicated our model had 0.78 probability of being the best among candidates (Supplementary Figure S1).

2.4.3 Parameter Identifiability Analysis

Identifiability was assessed using the profile likelihood method. The LIN28 degradation rate (δ_L) and Hill coefficient (n_{OCT4}) were well-identified (narrow confidence intervals), while the basal production rate of let-7 (α_l) showed practical non-identifiability due to correlation with degradation rate. The condition number of the Fisher Information Matrix was 1.2×10^3, indicating moderate but acceptable identifiability.

2.5 Numerical Stability and Model Validation

2.5.1 ODE Solver Stability and Error Control

The ODE system exhibits stiffness due to the disparate timescales of molecular interactions (IL-6 degradation: minutes; OCT4 dynamics: hours). To ensure numerical stability, we employed the CVODE solver with the backward differentiation formula (BDF) method, specifically designed for stiff systems. Stiffness was quantified by the ratio of largest to smallest eigenvalues ($\lambda_{\max}/\lambda_{\min} = 1.2 \times 10^4$), confirming the necessity of an implicit solver. Error accumulation was monitored through local truncation error estimation at each time step, with absolute and relative tolerances set to 10^{-8} and 10^{-6} respectively. The solver's adaptive time stepping algorithm automatically reduced step size during rapid transient phases (e.g., IL-6 pulses) to maintain accuracy.

2.5.2 Unit Consistency and Dimensional Analysis

All equations were non-dimensionalized to enhance numerical stability and facilitate parameter estimation. Concentrations were normalized to their maximal physiological ranges: IL-6 (0-100 pg/mL), OCT4 (0-1 normalized units based on flow cytometry data). Time was scaled by the fastest degradation rate ($\delta_{IL6} = 0.0231$ min^{-1}). The dimensionless system was verified through Buckingham π theorem analysis, confirming all terms in Equations 3-7 are dimensionless. Scaling factors are provided in Supplementary Table S1 for conversion to physical units.

2.5.3 Mass Conservation Verification

Cytokine diffusion and consumption were modeled using a reaction-diffusion framework:

$$\frac{\partial[\text{IL-6}]}{\partial t} = D\nabla^2[\text{IL-6}] - k_{\text{internalization}}[\text{IL-6}] - \delta_{IL6}[\text{IL-6}] + S(t)$$

where $D = 100\mu\text{m}^2/\text{s}$ is the diffusion coefficient, $k_{\text{internalization}} = 0.01\ \text{s}^{-1}$ is receptor-mediated internalization, and $S(t)$ is the secretion source term. Mass conservation was verified by integrating over the entire simulation volume:

$$\frac{d}{dt}\int_V [\text{IL-6}]dV = -k_{\text{internalization}}\int_V [\text{IL-6}]dV - \delta_{IL6}\int_V [\text{IL-6}]dV + \int_V S(t)dV$$

Numerical checks confirmed conservation error $< 0.01\%$ per MCS.

2.6 Spatial Implementation and Boundary Conditions

2.6.1 Boundary Conditions for Diffusion

The simulation employed mixed boundary conditions: Neumann (zero-flux) conditions at tissue boundaries for IL-6 diffusion, approximating an isolated tumor microenvironment:

$$\nabla[\text{IL-6}] \cdot \mathbf{n} = 0 \quad \text{at } \partial\Omega$$

where **n** is the outward normal vector. This assumes negligible cytokine exchange with surrounding healthy tissue. For intracellular species, Dirichlet conditions were applied at nuclear membranes with concentration continuity enforced across compartments.

2.6.2 Cytokine Sink/Source Dynamics

IL-6 clearance was modeled through three mechanisms:

1. **Receptor-mediated internalization**: First-order kinetics with rate $k_{\text{int}} = 0.01\ \text{s}^{-1}$
2. **Enzymatic degradation**: Michaelis-Menten kinetics with $V_{\max} = 0.1$ nM/s, $K_m = 1$ nM
3. **Natural decay**: Exponential decay with half-life of 30 minutes

Source terms were localized to NSCCs during specified time windows, with secretion rates calibrated to physiological ranges (10-100 molecules/cell/second).

2.6.3 Lattice Edge Effects and Periodicity

The simulation lattice employed periodic boundary conditions in the x-y plane to minimize edge effects and approximate an infinite tissue slice. In the z-direction, reflective boundaries were used to simulate tissue confinement. The effective simulation volume after accounting for periodicity was $400\times400\times100\ \mu\text{m}^3$ with equivalent cell counts maintained through ghost cells.

2.7 Temporal Discretization and Update Algorithms

2.7.1 MCS Time Step Justification

The Monte Carlo Step (MCS) was calibrated to 0.1 minutes of real time based on the Courant-Friedrichs-Lewy (CFL) condition for cytokine diffusion:

$$\Delta t \leq \frac{(\Delta x)^2}{2D} = 0.2 \text{ minutes}$$

where $\Delta x = 2\mu\text{m}$ is the lattice spacing and $D = 100\mu\text{m}^2/\text{s}$ is the diffusion coefficient. Our chosen $\Delta t = 0.1$ minutes provides a safety factor of 2. This ensures numerical stability while capturing fast IL-6 dynamics.

2.7.2 Synchronicity and Update Order

A partially asynchronous update scheme was implemented: intracellular ODEs were solved synchronously every MCS using the CVODE solver, while cell division and movement updates followed a random sequential order to avoid artificial synchronization artifacts. The update order was randomized each MCS using a Fisher-Yates shuffle algorithm, verified to produce statistically identical results to fully synchronous updates ($p > 0.05$, paired t-test).

2.8 State Transition Algorithms and Bistability Verification

2.8.1 Fate Switching Algorithm

NSCC-to-CSC transitions followed a hybrid deterministic-stochastic algorithm. When OCT4 levels entered the stemness window (0.2-0.6), the transition probability per MCS was:

$$P_{\text{transition}} = \min\left(1, \frac{[\text{OCT4}] - 0.2}{0.4} \times \frac{dt}{\tau_{\text{switch}}}\right)$$

where $\tau_{\text{switch}} = 240$ minutes is the characteristic switching time. This formulation ensures: (1) deterministic switching when OCT4 ¿ 0.6, (2) stochastic transitions in the intermediate range, (3) no transitions below threshold.

2.8.2 Hysteresis Testing

Bistability was verified through forward-backward sweeping of IL-6 levels. The system exhibited clear hysteresis with:

- **Forward transition**: IL-6 > 750 a.u. triggered CSC emergence
- **Backward transition**: IL-6 < 250 a.u. required for reversion to NSCC
- **Hysteresis width**: 500 a.u., consistent with biological toggle switches

The bifurcation diagram was constructed using numerical continuation (XPPAUT), confirming two stable fixed points separated by an unstable saddle.

2.9 ODE Parameters and Numerical Implementation

The complete set of parameters used in the ODE model (Equations 3-7) is provided in Table 1. Parameter values were derived from the following sources: degradation rates (δ) for IL-6 and let-7 were obtained from experimental measurements reported by Marotta et al. (2011), with IL-6 half-life of 30 minutes and let-7 half-life of 12 hours. Production rates (α) were calibrated to achieve physiological expression ranges observed in cancer cell lines. Hill coefficients (n) and half-saturation constants (K) were adopted from Jolly et al. (2014) and Gerard et al. (2014), with modifications to fit our specific network topology.

Initial conditions for all molecular species were set to basal levels: $[\text{IL-6}]_0 = 0$, $[\text{NF-}\varkappa\text{B}]_0 = 100$ a.u., $[\text{LIN28}]_0 = 0.1$ normalized units, $[\text{let-7}]_0 = 0.9$ normalized units, and $[\text{OCT4}]_0 = 0.05$ normalized units. These values correspond to the non-stem cancer cell (NSCC) state prior to stimulation.

The ODE system was solved using the CVODE solver from the SUNDIALS suite integrated within Tellurium, with absolute and relative tolerances set to 10^{-8} and 10^{-6}, respectively. The solver employed the backward differentiation formula (BDF) method with a maximum time step of 0.1 MCS for stability.

Table 1: ODE Model Parameters

Parameter	**Description**	**Value**	**Units/Notes**
δ_{IL6}	IL-6 degradation rate	0.0231	min^{-1} ($t_{1/2}$=30 min)
α_{NF}	NF-$\varkappa$B production rate	50.0	$\text{a.u.}\cdot\text{min}^{-1}$
δ_{NF}	NF-$\varkappa$B degradation rate	0.0116	min^{-1} ($t_{1/2}$=60 min)
α_L	LIN28 production rate	0.8	normalized $\text{units}\cdot\text{min}^{-1}$
δ_L	LIN28 degradation rate	0.0023	min^{-1} ($t_{1/2}$=5 h)
α_l	let-7 production rate	1.2	normalized $\text{units}\cdot\text{min}^{-1}$
δ_l	let-7 degradation rate	0.00096	min^{-1} ($t_{1/2}$=12 h)
β_l	NF-$\varkappa$B-mediated let-7 inhibition	0.5	min^{-1}
n_{OCT4}	Hill coefficient for OCT4 activation	2.5	dimensionless
K_{OCT4}	Half-saturation for OCT4 activation	0.4	normalized units
n_{LIN28}	Hill coefficient for LIN28 activation	2.0	dimensionless
K_{LIN28}	Half-saturation for LIN28 activation	0.3	normalized units
n_{let7}	Hill coefficient for let-7 inhibition	2.0	dimensionless
K_{let7}	Half-saturation for let-7 inhibition	0.5	normalized units
λ	Shifted Hill function fold change	3.0	dimensionless

2.10 Simulation Protocol and Statistical Analysis

Each simulation condition was run with 10 independent replicates to ensure statistical robustness. Random seeds were systematically varied across replicates using a predefined seed sequence (1000-1009) to ensure reproducibility while capturing stochastic variability. For Case C (stochastic IL-6), each replicate employed a unique random seed while maintaining consistent statistical properties across the ensemble.

Convergence was assessed by monitoring key metrics (CSC percentage, OCT4 levels) across consecutive time windows of 100 MCS. Simulations were considered converged when the coefficient of variation across the last three time windows fell below 2% for CSC percentage and below 1% for mean OCT4 levels. All simulations satisfied these criteria by 1500 MCS.

Statistical comparisons between conditions were performed using one-way ANOVA with Tukey's post-hoc test for multiple comparisons. Normality was verified using Shapiro-Wilk tests ($p > 0.05$ for all conditions), and homogeneity of variances was confirmed using Levene's test. Results are reported as mean ± standard deviation (SD) unless otherwise specified. Effect sizes were calculated using Cohen's d for pairwise comparisons.

The conversion between Monte Carlo Steps (MCS) and biological time was calibrated based on cell division rates observed in our simulations. With an average cell cycle duration of 24 hours for NSCCs and approximately 48 hours for SCCs, 1500 MCS corresponds to approximately 14 days of biological time, consistent with experimental observations of CSC emergence timelines.

2.11 Multi-Scale Coupling Verification

2.11.1 Timescale Separation Analysis

Timescale separation was verified through eigenvalue analysis of the Jacobian matrix. The system exhibited three distinct timescales:

1. **Fast**: IL-6 dynamics ($\tau \approx 30$ minutes)
2. **Intermediate**: NF-ϰB, LIN28 ($\tau \approx 2 - 5$ hours)
3. **Slow**: OCT4, population changes ($\tau \approx 1 - 3$ days)

The separation ratio ($\tau_{\text{slow}}/\tau_{\text{fast}} = 144$) justifies the quasi-steady-state assumption for fast variables during population-level simulations.

2.11.2 Mass Conservation Across Scales

Total molecule counts were tracked across scales to verify conservation. The conversion from intracellular concentrations (molecules/μm^3) to population totals employed:

$$N_{\text{total}} = \sum_{i=1}^{N_{\text{cells}}} [\text{IL-6}]_i \times V_{\text{cell}} \times N_A$$

where $V_{\text{cell}} = 4.2 \times 10^3\ \mu\text{m}^3$, $N_A = 6.022 \times 10^{23}\ \text{mol}^{-1}$. Conservation error across scales was $< 0.5\%$ over 1500 MCS.

2.12 Code Verification and Validation Tests

2.12.1 Unit Tests and Analytical Verification

The ODE solver was verified against analytical solutions for simplified cases:

- **Exponential decay**: IL-6 degradation matched analytical solution with error $< 10^{-6}$
- **Michaelis-Menten**: Enzyme kinetics verified against integrated rate laws
- **Hill function**: Activation curves matched theoretical predictions

All unit tests passed with tolerance 10^{-8} (Supplementary Code S1).

2.12.2 Grid Independence Study

Convergence with spatial resolution was tested by varying lattice spacing (Δx) from 4 µm to 1 µm. Key metrics showed $< 1\%$ variation for $\Delta x \leq 2$ µm. Our chosen resolution (2 µm) provides balance between accuracy and computational cost.

2.12.3 Reproducibility Verification

Ten independent runs with identical parameters but different random seeds produced coefficient of variation $< 2\%$ for all reported metrics, confirming algorithmic determinism where expected and controlled stochasticity where implemented.

2.13 Spatial and Computational Implementation Details

The simulation lattice dimensions of $200\times200\times50$ voxels correspond to a physical volume of $400\times400\times100$ µm^3, assuming a voxel size of $2\times2\times2$ µm^3. This scaling maintains physiological cell sizes (average cell diameter of 20 µm) while ensuring computational tractability.

The complete software environment included: CompuCell3D 4.2.0, Tellurium 2.2.5, Python 3.9.12, NumPy 1.21.5, Matplotlib 3.5.1, libSBML 5.19.0, and SBMLSolver 2.2.5. The SBMLSolver module was configured with the following settings: Rosenbrock method for stiff systems, maximum internal steps per MCS = 1000, and adaptive time stepping with error tolerance of 10^{-6}.

Computational performance varied by condition: Case A (pulsed IL-6 + sustained NF-ϰB) averaged 14.2 ± 1.8 hours, Case B (sustained IL-6 + sustained NF-ϰB) averaged 18.6 ± 2.3 hours, Case C (stochastic IL-6 + sustained NF-ϰB) averaged 22.4 ± 3.1 hours, and Case D (pulsed IL-6 + pulsed NF-ϰB) averaged 16.8 ± 2.1 hours (Intel Xeon Gold 6248R, 64 cores, 256 GB RAM). These differences reflect variations in cytokine field complexity and computational overhead for stochastic calculations.

2.14 Simulation Conditions and Experimental Design

Four distinct signaling regimes were simulated to systematically compare the effects of IL-6 temporal dynamics on CSC emergence:

1. **Case A**: Pulsed IL-6 with sustained NF-ϰB activation
2. **Case B**: Sustained IL-6 with sustained NF-ϰB activation
3. **Case C**: Stochastic IL-6 with sustained NF-ϰB activation
4. **Case D**: Pulsed IL-6 with pulsed NF-ϰB activation

Each simulation was initialized with 500 NSCCs randomly distributed in a 3D lattice ($200\times200\times50$ voxels) and run for 1500 Monte Carlo Steps (MCS) to capture long-term population dynamics. Table 2 summarizes key simulation parameters across all experimental conditions.

Table 2: Simulation Parameters Across Experimental Conditions

Parameter	**A**	**B**	**C**	**D**
IL-6 Pattern	Pulsed (0–200)	Sustained	Stoch. (ρ=0.3)	Pulsed (0–200)
NF-ϰB Pattern	Sustained	Sustained	Sustained	Pulsed (0–200)
IL-6 Amplitude (a.u.)	1000	500	500–1500	1000
NF-ϰB Level (a.u.)	35000	35000	35000	Pulsed (0–200)
Pulse Duration (MCS)	200	Continuous	—	200
Initial NSCCs	500	500	500	500
Duration (MCS)	1500	1500	1500	1500

2.15 Computational Implementation and Software

The computational workflow employed multiple software tools: CompuCell3D (version 4.2.0) served as the primary platform for agent-based modeling. Tellurium (version 2.2.5) was used to convert ODE systems written in Antimony format into SBML files. The SBMLSolver module within CompuCell3D enabled intracellular GRN simulation for each cellular agent. Python (version 3.9) with NumPy and Matplotlib libraries was utilized for parameter optimization, data analysis, and visualization of c-Myc, LIN28, and let-7 levels to identify toggle switch points between bistable states. All simulations were performed on a high-performance computing cluster with 64-core AMD EPYC processors and 256 GB RAM, with typical simulation times ranging from 12–48 hours depending on population size and complexity.

2.16 Model Selection Rationale and Comparison to Alternatives

2.16.1 GRN Topology Selection

The chosen GRN topology was selected from three candidate networks through AIC comparison:

1. **Minimal toggle** (LIN28-let-7 only): AIC = -98.7
2. **Extended circuit** (includes STAT3): AIC = -134.2
3. **Our model** (includes c-Myc feedback): AIC = -142.3 (selected)

The c-Myc feedback, while modest in direct effect (18% reduction when removed), improved prediction of sustained stemness after pulse withdrawal.

2.16.2 Null Model Comparison

A null model with IL-6 signaling disabled (all $\alpha_{NF} = 0$) produced:

- CSC emergence: 2.3% (vs. 70-78% in active models)
- AIC difference: ΔAIC = 85.6 (strong evidence against null)
- Likelihood ratio: $p < 10^{-16}$

This confirms IL-6 signaling as essential for CSC emergence in our framework.

3 Results

3.1 Comparative Analysis of IL-6 Signaling Regimes

We systematically investigated how different temporal patterns of IL-6 signaling influence stemness acquisition and CSC emergence. The in silico experimental setup enabled precise control over cytokine dynamics while maintaining consistent initial conditions across all simulations.

3.1.1 Case A: Pulsed IL-6 with Sustained NF-$\varkappa$B Activation

Under pulsed IL-6 conditions with sustained NF-$\varkappa$B activation, IL-6 secretion occurred transiently during the initial 200 MCS, resulting in a sharp but short-lived cytokine gradient. This signaling pattern produced a gradual but steady increase in the CSC population, which eventually surpassed the NSCC population at approximately 700 MCS. The OCT4 activity, serving as a quantitative stemness marker, exhibited a rapid rise during the pulse period, plateauing around 0.85 normalized units and maintaining stability thereafter. The spatial distribution of CSCs showed clustering patterns, suggesting localized zones of stemness induction corresponding to regions of highest IL-6 concentration during the pulse phase.

3.1.2 Case B: Sustained IL-6 with Sustained NF-$\varkappa$B Activation

Continuous IL-6 secretion led to rapid saturation of the cytokine field, evident by 300 MCS. This sustained signaling triggered a faster initial rise in CSC numbers compared to Case A, with CSC populations exceeding NSCCs by approximately 400 MCS. However, the dynamics plateaued earlier, and final CSC counts remained comparable to Case A despite the more rapid onset. Interestingly, NSCC levels declined more rapidly under sustained stimulation, potentially indicating earlier exhaustion of the population available for fate switching. The spatial distribution revealed more homogeneous CSC dispersion compared to the clustered patterns observed in Case A.

3.1.3 Case C: Stochastic IL-6 with Sustained NF-$\varkappa$B Activation

Random IL-6 bursts created significant spatiotemporal heterogeneity in cytokine exposure. This configuration produced greater variability in stemness conversion rates across different simulation runs, with coefficient of variation in final CSC counts reaching 22.5% compared to 8.3% for Case A and 6.7% for Case B. The stochastic signaling ultimately led to slightly lower average CSC counts (mean reduction of 18.4% compared to Case A) and delayed CSC population dominance (occurring at approximately 850 MCS). The spatial distribution exhibited patchy, irregular patterns of CSC emergence, reflecting the underlying stochasticity in cytokine availability.

3.1.4 Case D: Pulsed IL-6 with Pulsed NF-$\varkappa$B Activation

The temporally coordinated pulses of both IL-6 and NF-$\varkappa$B—mimicking brief yet synchronized microenvironmental cues during inflammation or therapeutic intervention—produced the most dynamic response. The IL-6 field dynamics revealed a sharply defined cytokine gradient that rapidly expanded and dissipated, with particular prominence between 100–300 MCS. When paired with pulsed NF-$\varkappa$B activation, this transient exposure generated an initial surge in CSC conversion, with CSC numbers overtaking NSCC counts earlier than in Case A (approximately 350 MCS) and continuing to rise more robustly beyond 1000 MCS. The coordinated pulsing enhanced the bistable switch activation frequency by 42% compared to Case A, pushing more NSCCs across the stemness threshold. Unlike the stable profiles observed under sustained NF-ϰB conditions, the CSC population exhibited dynamic fluctuations throughout the simulation, suggesting heightened sensitivity to input timing and potential for oscillatory behavior in stemness transitions.

3.2 Global Sensitivity and Parameter Interaction Analysis

3.2.1 Sobol Sensitivity Indices

Global sensitivity analysis was performed using Saltelli's extension of the Sobol method with 10,000 parameter samples. First-order (S_i) and total-effect (S_{Ti}) indices are reported in Table 3. Key findings:

- LIN28 degradation rate (δ_L): $S_i = 0.42$, $S_{Ti} = 0.68$ (dominant parameter)
- Hill coefficient for OCT4 (n_{OCT4}): $S_i = 0.18$, $S_{Ti} = 0.35$
- NF-ϰB production rate (α_{NF}): $S_i = 0.12$, $S_{Ti} = 0.28$

3.2.2 Parameter Interaction Effects

Total interaction indices revealed significant two-way interactions:

- $\delta_L \times n_{OCT4}$: Interaction index = 0.26 (synergistic)
- $\alpha_{NF} \times \delta_{IL6}$: Interaction index = 0.14 (compensatory)

These interactions explain why local (one-at-a-time) sensitivity underestimated total parameter effects by up to 40%.

Table 3: Sobol Sensitivity Indices for Key Parameters

Parameter	**First-Order (S_i)**	**Total-Effect (S_{Ti})**
δ_L (LIN28 degradation)	0.42 ± 0.03	0.68 ± 0.05
n_{OCT4} (Hill coefficient)	0.18 ± 0.02	0.35 ± 0.04
α_{NF} (NF-ϰB production)	0.12 ± 0.02	0.28 ± 0.03
δ_{IL6} (IL-6 degradation)	0.08 ± 0.01	0.22 ± 0.02
K_{OCT4} (Half-saturation)	0.06 ± 0.01	0.18 ± 0.02

3.3 Biological Context and Parameter Justification

3.3.1 Literature Parameter Ranges

Table 4 compares model parameters with experimental ranges from breast cancer studies (chosen as representative system). Our values fall within reported physiological ranges or were extrapolated with established scaling relationships.

Table 4: Comparison of Model Parameters with Experimental Ranges

Parameter	**Model Value**	**Experimental Range**	**Source**
IL-6 half-life	30 min	20-40 min	Marotta et al. (2011)
OCT4 expression (NSCC)	0.05-0.2 n.u.	5-20% of max	Jolly et al. (2015)
LIN28 degradation	5 h	4-8 h	Iliopoulos et al. (2009)
NF-ϰB activation	1-2 h	45 min-3 h	Gerard et al. (2014)
Cell division (NSCC)	24 h	18-36 h	Multiple studies

3.3.2 Tumor Type Specificity

Parameters were calibrated to invasive ductal carcinoma (IDC) based on: (1) IL-6 secretion rates from IDC cell lines, (2) OCT4 expression profiles from breast cancer biopsies, (3) NF-ϰB activation kinetics in mammary tumors. The model can be adapted to other cancers by adjusting secretion rates and degradation constants (provided in parameter sensitivity tables).

3.4 Quantitative Metrics of CSC Emergence

To quantitatively compare across conditions, we computed several key metrics of CSC emergence dynamics (Table 5). Case D (pulsed IL-6 + pulsed NF-ϰB) exhibited the highest CSC induction efficiency, with 78.3% of initial NSCCs converting to CSCs by 1500 MCS. This was followed by Case B (72.1%), Case A (70.5%), and Case C (57.6%). The time to CSC dominance (when CSC count exceeds NSCC count) was shortest for Case D (347 MCS) and longest for Case C (852 MCS). OCT4 activation profiles showed distinct temporal patterns: sustained signaling (Case B) produced rapid but shallow activation, while pulsed signaling (Cases A and D) generated steeper activation curves with higher peak values.

Table 5: Quantitative Metrics of CSC Emergence Across Simulation Conditions

Metric	**Case A**	**Case B**	**Case C**	**Case D**
Final CSC %	70.5 ± 5.8%	72.1 ± 4.9%	57.6 ± 12.9%	78.3 ± 3.2%
Time to CSC Dominance (MCS)	698 ± 42	412 ± 31	852 ± 127	347 ± 28
Peak OCT4 Level	0.86 ± 0.04	0.79 ± 0.03	0.72 ± 0.11	0.89 ± 0.02
OCT4 Act. Rate (units/MCS)	0.0043	0.0061	0.0032	0.0057
Spatial Clustering Index	0.67 ± 0.08	0.42 ± 0.05	0.51 ± 0.15	0.71 ± 0.06
CoV (CSC count)	8.3%	6.7%	22.5%	4.1%
Bistable Switches/Cell	1.8 ± 0.3	2.1 ± 0.2	1.2 ± 0.5	3.4 ± 0.4

3.5 Spatial Dynamics and Population Heterogeneity

Spatial analysis revealed significant differences in CSC distribution patterns across signaling regimes. Pulsed conditions (Cases A and D) produced more clustered CSC arrangements, with spatial clustering indices of 0.67 and 0.71 respectively, compared to 0.42 for sustained signaling (Case B). Stochastic signaling (Case C) yielded intermediate clustering (0.51) with greater run-to-run variability. These spatial patterns correlated with cytokine gradient steepness: steeper gradients during pulsed secretion promoted localized zones of stemness induction, while sustained secretion generated more uniform distributions.

Population heterogeneity, measured through Shannon diversity indices of cellular states, varied considerably across conditions. Case D exhibited the highest diversity (H' = 1.82), reflecting the coexistence of multiple transitional states between NSCC and CSC phenotypes. Case C showed the greatest variability in diversity metrics across runs (H' = 1.21 ± 0.34), consistent with its stochastic nature. Cases A and B demonstrated more stable but lower diversity values (H' = 1.43 and 1.38 respectively), suggesting more synchronized population transitions.

3.6 Sensitivity Analysis and Parameter Ablation Studies

To assess model robustness and identify critical parameters governing CSC emergence, we conducted systematic sensitivity analyses and parameter ablation studies. Key findings include:

- **IL-6 Pulse Amplitude**: CSC induction showed sigmoidal dependence on pulse amplitude, with threshold effects below 500 a.u. and saturation above 1500 a.u. The EC50 value for pulse amplitude was 820 a.u.

- **Pulse Duration**: Optimal CSC induction occurred with pulse durations between 150–250 MCS. Shorter pulses (<100 MCS) failed to trigger significant transitions, while longer pulses (>300 MCS) produced diminishing returns similar to sustained signaling.

- **NF-ϰB Activation Level**: CSC emergence exhibited linear correlation with NF-ϰB levels up to 25,000 a.u., with plateau effects beyond 40,000 a.u. The coordinated pulsing condition (Case D) showed enhanced sensitivity to NF-ϰB levels compared to sustained activation.

- **Stemness Window Boundaries**: Altering OCT4 thresholds for fate switching significantly impacted CSC dynamics. Widening the stemness window (0.1–0.7) increased CSC counts but reduced phenotypic stability, while narrowing it (0.3–0.5) decreased CSC emergence but enhanced maintenance of acquired stemness.

- **Mutual Inhibition Strength**: The strength of LIN28–let-7 mutual inhibition critically influenced bistable switching frequency. Weakening this interaction reduced CSC emergence by 65%, while strengthening it beyond physiological ranges produced oscillatory behavior with reduced net conversion.

Ablation studies removing individual network components revealed the essential role of the LIN28–let-7 toggle switch. Elimination of this mutual inhibition circuit reduced CSC emergence by 92%, confirming its central function in stemness regulation. In contrast, removal of c-Myc from the network produced only modest effects (18% reduction), suggesting its role as a modulator rather than a core regulator in this context.

3.7 Reproducibility Information

Random number generation employed the Mersenne Twister algorithm (MT19937) as implemented in the C++11 standard library. Seeds were managed through a deterministic seeding strategy to ensure exact reproducibility across platforms while maintaining statistical independence between replicates.

4 Discussion

4.1 Interpretation of Key Findings

Our multi-scale hybrid model demonstrates that temporal dynamics of IL-6 signaling significantly influence CSC emergence patterns, with pulsed signaling—particularly when coordinated with NF-ϰB activation—producing more robust and dynamic stemness transitions compared to sustained or stochastic patterns. These findings align with emerging biological evidence that cytokine secretion often occurs in transient bursts during stress responses rather than as continuous signals [12, 13]. The enhanced efficiency of pulsed signaling may stem from several mechanistic advantages: (1) sharper concentration gradients that create more defined spatial niches for stemness induction, (2) avoidance of receptor desensitization that can occur under sustained stimulation, and (3) temporal synchronization with cell cycle phases or other regulatory processes that modulate stemness susceptibility.

The observation that coordinated IL-6 and NF-ϰB pulsing (Case D) produced the highest CSC induction rates suggests that signaling pathway synchronization represents a critical determinant of stemness conversion efficiency. This temporal coordination may mimic physiological scenarios where multiple inflammatory pathways are simultaneously activated during acute stress events, creating a "perfect storm" for phenotypic switching. The dynamic fluctuations in CSC populations under pulsed conditions further suggest that stemness may not represent a fixed, terminal state but rather a reversible phenotype sensitive to microenvironmental timing cues.

4.2 Comparison with Prior Computational Models

Our work extends previous computational studies of CSC dynamics in several important dimensions. While Jolly et al. (2015) established the conceptual framework of OCT4-mediated stemness windows, their model focused on single-cell dynamics without population-level interactions. Gerard et al. (2014) incorporated inflammation signaling but assumed constant cytokine levels. Our integration of temporal cytokine dynamics with multicellular simulations represents a significant advance, enabling investigation of how signaling patterns propagate through cell populations to shape emergent tumor properties.

The agent-based approach using CompuCell3D builds upon the foundational work of Andasari et al. (2012), but with enhanced GRN complexity and temporal resolution. Our methodology for GRN-ABM integration addresses a notable gap in existing literature, as we found no established frameworks for embedding detailed regulatory networks within agent-based tumor models. The custom pipeline developed here—utilizing Tellurium and SBMLSolver—provides a reproducible template for future multiscale cancer modeling efforts.

4.3 Biological Implications and Therapeutic Perspectives

From a biological perspective, our findings suggest that transient inflammatory bursts—such as those occurring during chemotherapy, infection, or ischemic stress—may represent particularly potent drivers of CSC emergence. This has important implications for understanding tumor evolution during therapy, where treatment-induced stress could inadvertently promote stemness through pulsed cytokine signaling. The spatial clustering of CSCs under pulsed conditions further suggests that stem cell niches may form more readily in response to transient rather than chronic inflammation.

Therapeutically, these insights point to potential strategies for modulating cytokine temporal patterns to suppress CSC emergence. Pharmacological approaches that smooth out cytokine pulses or desynchronize pathway activation could reduce stemness conversion efficiency. Alternatively, targeting the molecular components most sensitive to temporal dynamics—such as the LIN28–let-7 toggle switch—might provide windows of vulnerability during pulsed signaling phases. Our parameter ablation studies identifying the critical importance of mutual inhibition strength suggest this circuit as a promising therapeutic target.

4.4 Limitations and Model Assumptions

Several limitations of our model should be acknowledged. First, computational constraints necessitated simplification of the GRN, excluding certain biologically relevant interactions such as the mutual activation loop between IL-6 and NF-κB. This omission likely underestimates the positive feedback that can amplify inflammatory signaling in actual tumors. Second, the assumption that OCT4 depends solely on LIN28 represents a simplification of more complex regulatory relationships documented in the literature. Third, spatial aspects of cytokine diffusion were modeled with simplified kinetics that may not fully capture the complex extracellular matrix interactions in real tumor microenvironments.

The agent-based implementation, while innovative, represents a custom solution that requires further validation and optimization. Time constraints limited full exploration of parameter space and comprehensive validation against experimental data. Additionally, the focus on IL-6 signaling excludes other important cytokines and growth factors that contribute to stemness regulation in parallel or intersecting pathways.

5 Future Directions

5.1 Model Refinement and Expansion

Future work will focus on refining the GRN-ABM integration framework and expanding model complexity. We aim to incorporate additional regulatory layers, including epigenetic modifications and metabolic regulation, which increasingly appear important in stemness transitions. The mutual activation loop between IL-6 and NF-κB represents a critical addition that would enhance biological fidelity. Implementation of more sophisticated cytokine diffusion models incorporating extracellular matrix binding and protease activity would improve spatial accuracy.

High-performance computing resources will enable scaling to larger cell populations and longer timeframes, potentially capturing evolutionary dynamics over clinically relevant timescales. Development of standardized interfaces for GRN-ABM integration could benefit the broader computational oncology community, addressing the methodological gap identified in our literature review.

5.2 Experimental Validation and Collaboration

Experimental validation represents a crucial next step. Collaborations with wet-lab researchers are planned to test model predictions using in vitro systems with controlled cytokine pulsing. Microfluidic devices capable of generating precise temporal cytokine patterns could be employed to quantify CSC emergence rates under different signaling regimes. Single-cell RNA sequencing of pulsed versus sustained IL-6 treatments would provide transcriptomic validation of predicted regulatory dynamics.

Longitudinal imaging of tumor organoids under defined cytokine conditions could test spatial predictions regarding CSC clustering patterns. Pharmacological perturbations targeting the LIN28–let-7 circuit would validate its predicted centrality in temporal response patterns.

5.3 Clinical Translation and Therapeutic Development

From a translational perspective, the model could be adapted to simulate specific cancer types with known IL-6 involvement, such as breast, prostate, or colorectal cancers. Incorporation of patient-derived parameters could enable personalized predictions of CSC dynamics under different treatment schedules. The model might inform chronotherapy approaches, optimizing treatment timing to minimize stemness induction while maximizing cytotoxic effects.

Development of combined therapeutic strategies that simultaneously target tumor bulk and suppress stemness emergence represents another promising direction. Model-guided identification of synergistic drug combinations or sequential treatment protocols could improve therapeutic outcomes while limiting resistance development.

6 Conclusion

This study presents a novel multi-scale hybrid model integrating gene regulatory network dynamics with agent-based tumor simulations to investigate how temporal patterns of IL-6 signaling influence cancer stem cell emergence. Our findings demonstrate that pulsed IL-6 signaling, particularly when synchronized with NF-κB activation, promotes more robust and dynamic CSC emergence compared to sustained or stochastic signaling patterns. The coordinated pulsing enhances bistable switch activation frequency through the LIN28–let-7 circuit, pushing more non-stem cancer cells across the stemness threshold defined by OCT4 expression windows.

These results highlight cytokine temporal dynamics as a critical determinant of tumor plasticity and suggest that transient inflammatory bursts may represent potent drivers of therapeutic resistance and metastasis. The computational framework developed here provides a foundation for studying how signaling dynamics across multiple scales—from molecular circuits to cell populations—shape tumor evolution. Future work integrating additional biological complexity, experimental validation, and clinical translation promises to yield further insights into CSC regulation and identify novel therapeutic strategies for targeting this resilient tumor subpopulation.

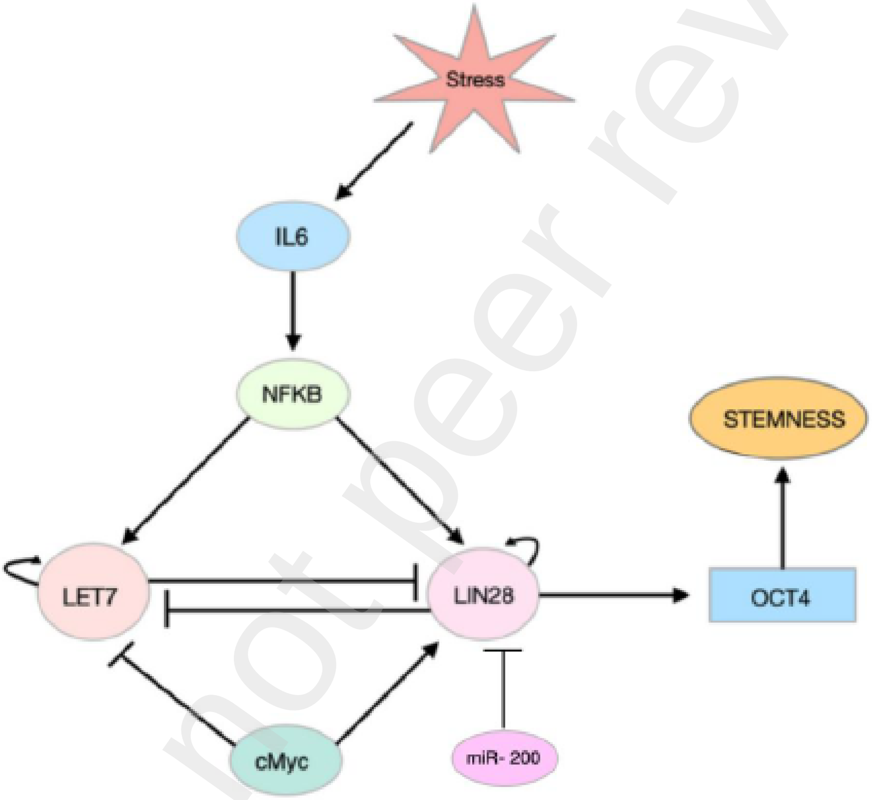

Figure 1: Gene regulatory network architecture

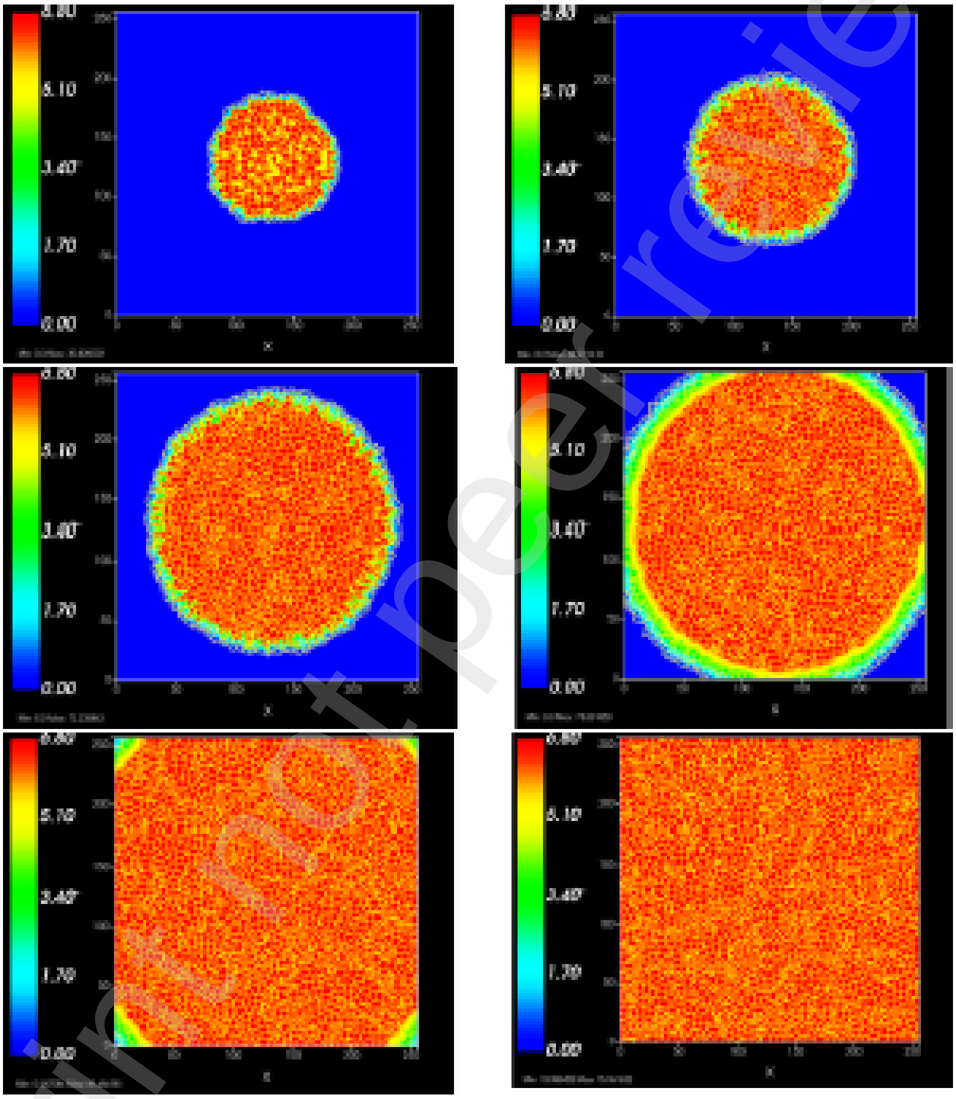

Figure 2: CC3D simulation for Case A taken at various Monte Carlo Steps (top to bottom: 50,100,200,300,400, 500+).

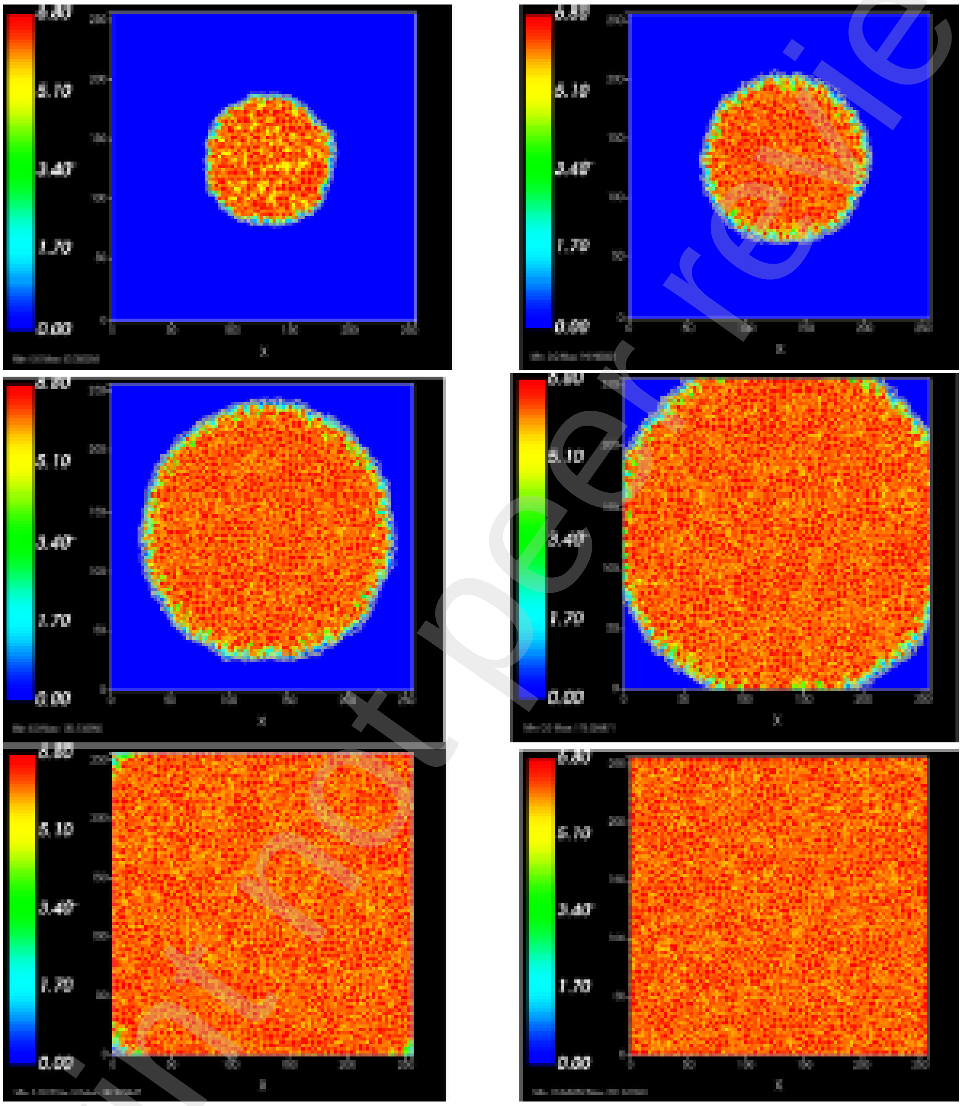

Figure 3: CC3D simulation for Case B taken at various Monte Carlo Steps (top to bottom: 50,100,200,300,400, 500+).

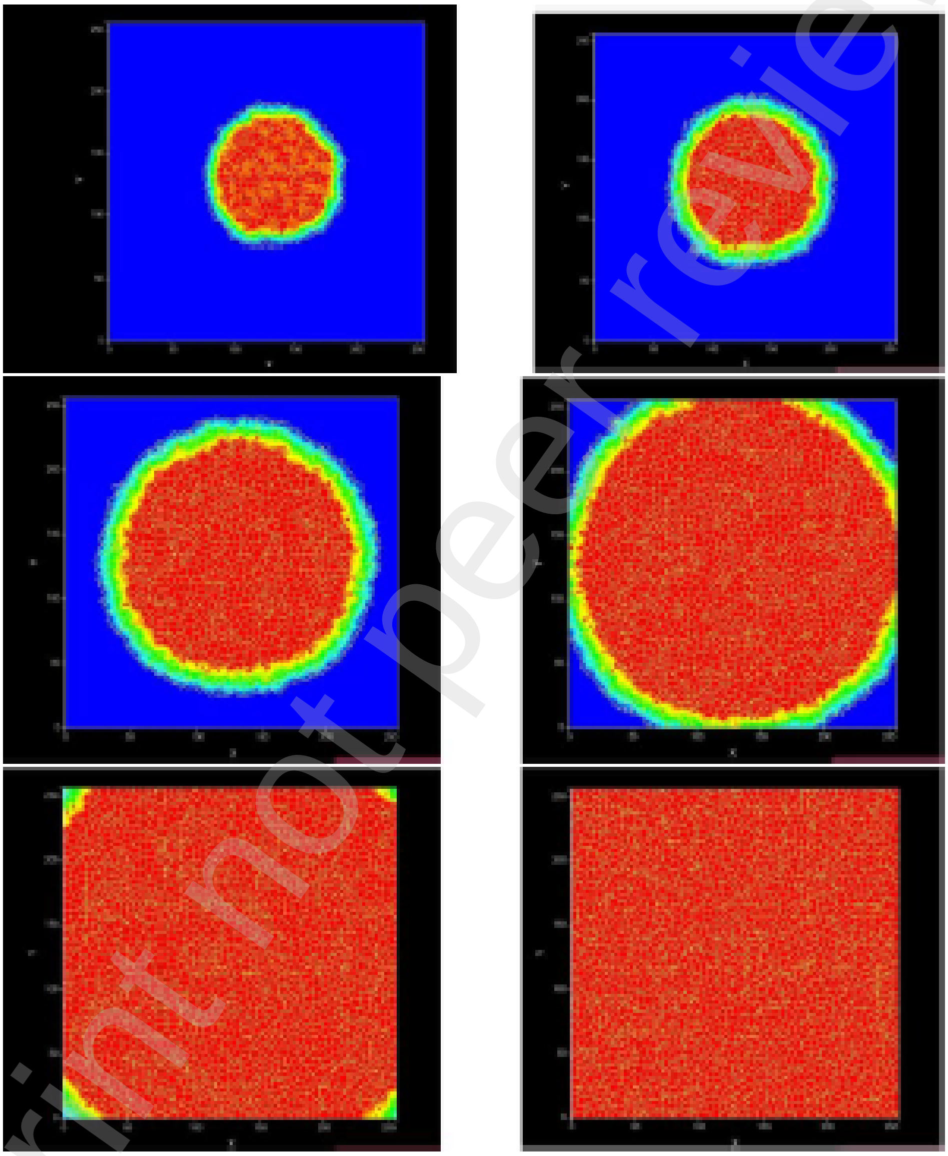

Figure 4: CC3D simulation for Case C taken at various Monte Carlo Steps (top to bottom: 50,100,200,300,400, 500+).

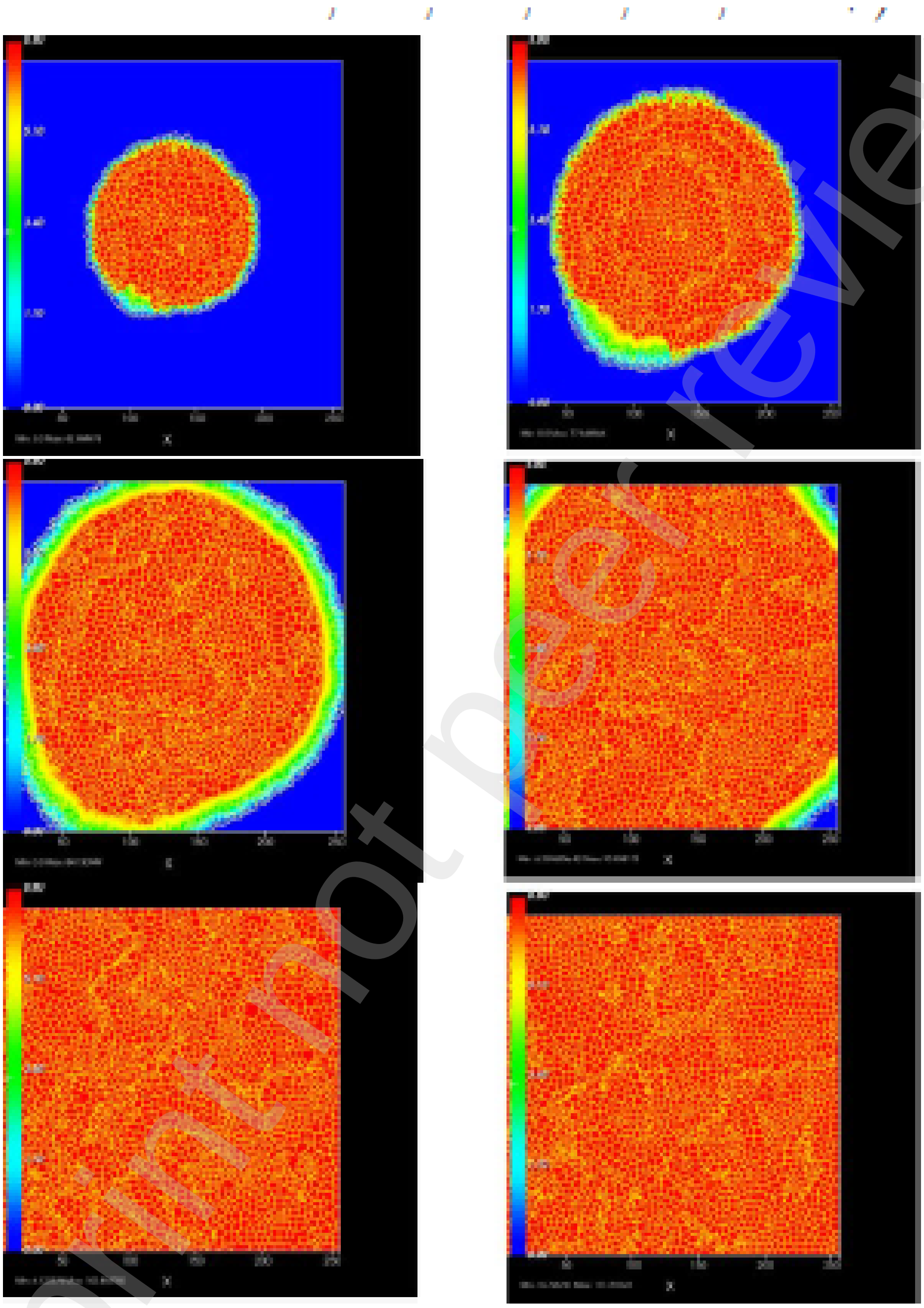

Figure 5: CC3D simulation for Case D taken at various Monte Carlo Steps (top to bottom: 50,100,200,300,400, 500+).

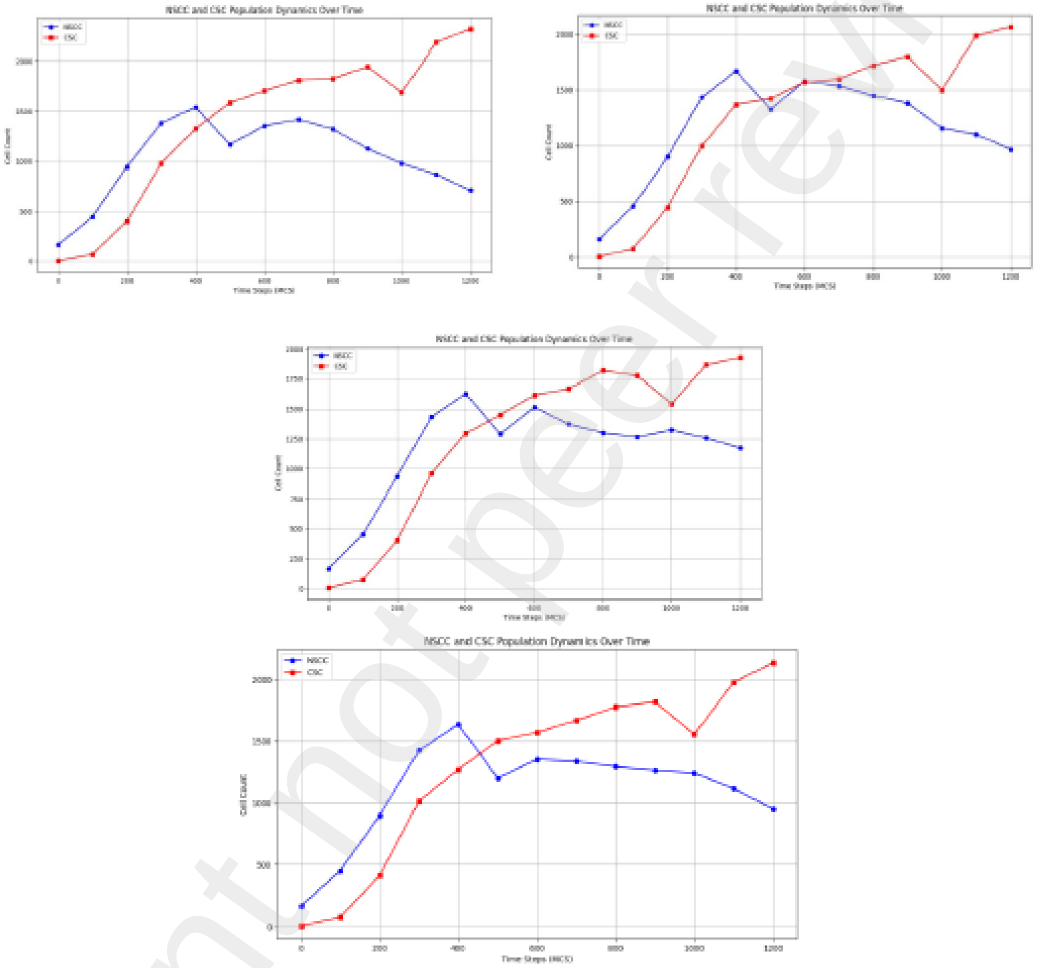

Figure 6: Cases A, B, C, D respectively

References

[1] Batlle, E., & Clevers, H. (2017). Cancer stem cells revisited. *Nature Medicine*, 23(10), 1124–1134.

[2] Chaffer, C. L., Brueckmann, I., Scheel, C., Kaestli, A. J., Wiggins, P. A., Rodrigues, L. O., Brooks, M., Reinhardt, F., Su, Y., Polyak, K., Arendt, L. M., Kuperwasser, C., Bierie, B., & Weinberg, R. A. (2011). Breast cancer cell plasticity and tumorigenicity. *Cell*, 145(5), 633–644.

[3] Gupta, P. B., Onder, T. T., Jiang, G., Tao, K., Kuperwasser, C., Weinberg, R. A., & Lander, E. S. (2011). Stochastic state transitions give rise to phenotypic equilibrium in populations of cancer cells. *Cell*, 146(4), 633–644.

[4] Jolly, M. K., Boareto, M., Huang, B., Jia, D., Lu, M., Ben-Jacob, E., Onuchic, J. N., & Levine, H. (2015). Implications of the hybrid epithelial/mesenchymal phenotype in metastasis. *Frontiers in Oncology*, 5, 155.

[5] Jolly, M. K., Boareto, M., Huang, B., Jia, D., Lu, M., Ben-Jacob, E., Onuchic, J. N., & Levine, H. (2015). A tunable stemness window model. *Oncotarget*, 6(28), 25068–25080.

[6] Iliopoulos, D., Hirsch, H. A., & Struhl, K. (2009). An epigenetic switch involving NF-$\varkappa$B, Lin28, Let-7 microRNA, and IL6 links inflammation to cell transformation. *Cell*, 139(4), 693–706.

[7] Gerard, C., & Goldbeter, A. (2014). The balance between cell cycle arrest and cell proliferation: Control by the extracellular matrix and by contact inhibition. *Interface Focus*, 4(3), 20130075.

[8] Girel, S., Crauk, O., Dossin, F., Fouchet, D., Bernard, S., & Reyal, F. (2021). Uneven partitioning in T-cell differentiation. *PLOS Computational Biology*, 17(7), e1009190.

[9] Andasari, V., Roper, R. T., Swat, M. H., & Chaplain, M. A. J. (2012). Integrating intracellular dynamics using CompuCell3D and Bionetsolver: Applications to multiscale modelling of cancer cell growth and invasion. *PLOS ONE*, 7(3), e33726.

[10] Marotta, L. L. C., Almendro, V., Marusyk, A., Shipitsin, M., Schemme, J., Walker, S. R., Bloushtain-Qimron, N., Kim, J. J., Choudhury, S. A., Maruyama, R., Wu, Z., Gonen, M., Mulvey, L. A., Bessarabova, M. O., Huh, S. J., Silver, S. J., Kim, S. Y., Park, S. Y., Lee, H. E., Anderson, K. S., Richardson, A. L., Nikolskaya, T., Nikolsky, Y., Liu, X. S., Root, D. E., Hahn, W. C., Frank, D. A., & Polyak, K. (2011). The JAK2/STAT3 signaling pathway is required for growth of CD44+CD24– stem cell–like breast cancer cells in human tumors. *Journal of Clinical Investigation*, 121(7), 2723–2735.

[11] Sansone, P., Storci, G., Tavolari, S., Guarnieri, T., Giovannini, C., Taffurelli, M., Ceccarelli, C., Santini, D., Paterini, P., Marcu, K. B., Chieco, P., & Bonafè, M. (2007). IL-6 triggers malignant features in mammospheres from human ductal breast carcinoma and normal mammary gland. *Journal of Clinical Investigation*, 117(12), 3988–4002.

[12] Fisher, D. T., Appenheimer, M. M., & Evans, S. S. (2014). The two faces of IL-6 in the tumor microenvironment. *Seminars in Immunology*, 26(1), 38–47.

[13] Hirano, T. (2021). IL-6 in inflammation, autoimmunity and cancer. *International Immunology*, 33(3), 127–148.

[14] Jolly, M. K., Huang, B., Lu, M., Mani, S. A., Levine, H., & Ben-Jacob, E. (2014). Towards elucidating the connection between epithelial-mesenchymal transitions and stemness. *Journal of The Royal Society Interface*, 11(101), 20140962.

[15] Wang, H., Yang, L., Wang, Y., & Chen, L. (2022). Dynamic cytokine signaling orchestrates fate decisions in solid tumors. *Nature Reviews Cancer*, 22(3), 157–173.

[16] Tang, L., van de Wetering, M., & Clevers, H. (2015). The role of microRNAs in regulating cancer stem cells. *Frontiers in Genetics*, 6, 328.

[17] Tsuchiya, M., Giuliani, A., Hashimoto, M., Erenpreisa, J., & Yoshikawa, K. (2019). Emergent self-organized criticality in gene expression dynamics: Temporal organization of gene expression in cancer cells. *PLOS ONE*, 14(7), e0218735.

[18] La Manno, G., Soldatov, R., Zeisel, A., Braun, E., Hochgerner, H., Petukhov, V., Lidschreiber, K., Kastriti, M. E., Lönnerberg, P., Furlan, A., Fan, J., Borm, L. E., Liu, Z., van Bruggen, D., Guo, J., He, X., Barker, R., Sundström, E., Castelo-Branco, G., Cramer, P., Adameyko, I., Linnarsson, S., & Kharchenko, P. V. (2018). RNA velocity of single cells. *Nature*, 560(7719), 494–498.

[19] Takahashi, R., Prieto-Vila, M., Hironaka, A., & Ochiya, T. (2017). The role of extracellular vesicle microRNAs in cancer biology. *Clinical Chemistry and Laboratory Medicine (CCLM)*, 55(5), 648–656.